Correlated sequential tunneling through a double barrier for interacting one-dimensional electrons

M. Thorwart[1], R. Egger[1], and M. Grifoni[2]
[1] *Institut für Theoretische Physik, Heinrich-Heine-Universität Düsseldorf, D-40225 Düsseldorf, Germany*
[2] *Institut für Theoretische Physik, Universität Regensburg, D-93040 Regensburg, Germany*
(Dated: February 2, 2008)

The problem of resonant tunneling through a quantum dot weakly coupled to spinless Tomonaga-Luttinger liquids has been studied. We compute the linear conductance due to sequential tunneling processes upon employing a master equation approach. Besides the previously used lowest-order golden rule rates describing uncorrelated sequential tunneling (UST) processes, we systematically include higher-order correlated sequential tunneling (CST) diagrams within the standard Weisskopf-Wigner approximation. We provide estimates for the parameter regions where CST effects can be important. Focusing mainly on the temperature dependence of the peak conductance, we discuss the relation of these findings to previous theoretical and experimental results.

PACS numbers: 05.60.Gg, 71.10.Pm, 73.63.-b

I. INTRODUCTION

The startling properties of one-dimensional (1D) interacting electrons, commonly referred to as (non-chiral) Tomonaga-Luttinger liquid (TLL) behavior,[1,2] see Refs. 3,4 for reviews, have recently moved into the focus of attention of the mesoscopic physics community. This was in particular prompted by the successful demonstration of electrical transport experiments for a variety of 1D materials, such as semiconductor quantum wires,[5] fractional quantum Hall edge states,[6] and single-wall carbon nanotubes (SWNTs).[7] In this paper, we mainly focus on electrical transport in SWNTs to keep the discussion concrete. Nevertheless, our results apply also to other systems. Shortly after the theoretical proposal of TLL behavior in individual metallic SWNTs,[8,9] the first experimental evidence for this peculiar many-body state was reported.[10,11,12,13] The expected TLL power-law scaling in the energy-dependent tunneling density of states[14] in SWNTs has been verified experimentally. In later experiments,[15,16] transport through an intrinsic quantum dot formed by a double barrier within the SWNT has been probed, allowing one to study the well-known resonant or sequential tunneling including Coulomb blockade phenomena,[17,18,19] but now for the case of leads formed by strongly correlated electrons. When varying an externally applied gate voltage, the linear conductance then typically displays a sequence of peaks, which can be interpreted as Coulomb oscillations or resonant tunneling peaks, depending on the parameter regime. The peak spacing is governed by the charging energy E_c and the plasmon level spacing ε on the dot (the latter coincides with the single-particle level spacing E_s for the case of noninteracting electrons). We mention in passing that a similar double-barrier experiment has been performed for semiconductor quantum wires, where in fact a TLL power-law temperature dependence of the peak conductance was reported.[5] In the nanotube experiments,[15,16] two intramolecular barriers have been created within an individual metallic SWNT, and a power-law temperature dependence of the conductance maximum has been reported.[15] However, the exponent turned out to be inconsistent with expectations based on the sequential tunneling theory for a TLL; see below. The experiments clearly indicate that a detailed theoretical understanding of transport through a double barrier in a TLL is required.

Since the initial theoretical work on this topic,[14,20] the double-barrier problem in a TLL has attracted a significant amount of attention among theorists.[21,22,23,24,25,26,27,28,29] Those works show that the electron-electron interactions present in 1D leads imply significant deviations from the conventional theory for Fermi liquid leads.[17,18] This is most easily seen through the change of the temperature dependence of the linear conductance peak height, which now exhibits a typical TLL power law $G_{\max}(T) \propto T^{\alpha}$, where α depends on the interaction strength. As is discussed in detail below, for a TLL, the exponent α reveals the particular tunneling mechanism ruling transport through the dot. SWNTs possess an additional flavor degeneracy,[8,9] which (together with the spin degree of freedom) can be captured by an effective four-channel TLL model. For an analysis of the linear conductance on resonance, which is the focus of our work, however, a spinless single-channel TLL turns out to be sufficient.[14,22,28] Within the standard bosonization method,[3] the TLL is then characterized by a boson field $\vartheta(x)$ with conjugate momentum $\Pi(x)$. Including a symmetric double barrier, composed of short-range scattering centers at $\pm x_0/2$ of strength $U_{\rm imp}$, the basic Hamiltonian is[14,20]

$$H = \frac{v_F}{2}\int dx \left\{\Pi^2 + \frac{1}{g^2}(\partial_x\vartheta)^2\right\} + H_{\rm imp} + H_{\rm ext}, \quad (1)$$

where v_F is the Fermi velocity,

$$H_{\rm imp} = U_{\rm imp}\sum_{\pm}\cos[\sqrt{4\pi}\vartheta(\pm x_0/2)],$$

and we put $\hbar = k_B = 1$ throughout this paper. Asymmetric barriers can also be studied using our approach

below, but to keep the discussion as simple as possible, we restrict ourselves to the symmetric case alone. The electron-electron interaction strength in the leads is measured in terms of the standard dimensionless TLL parameter g, where $g = 1$ for a Fermi gas and $g < 1$ for repulsive interactions.[3,4] We then have an intrinsic quantum dot within the TLL, with a plasmon level spacing $\varepsilon = E_s/g$, where $E_s = \pi v_F/x_0$ is the single-particle level spacing, and a charging energy $E_c = E_s/g^2$. (Note that our convention for E_c differs from the standard one.[19]) Finally, the coupling to an applied bias voltage V and to an external gate voltage V_G, acting onto the dot's electrons via a capacitance $C_{\rm G}$, is encoded in[14,20]

$$H_{\rm ext} = -e(VN/2 + cV_G n), \tag{2}$$

where $c = C_G/(C + C_G)$ with the island capacitance C. In Eq. (2), we used the notation

$$\begin{aligned} N &= \frac{1}{\sqrt{\pi}}\left[\vartheta\left(\frac{x_0}{2}\right) + \vartheta\left(-\frac{x_0}{2}\right)\right], \\ n &= \frac{1}{\sqrt{\pi}}\left[\vartheta\left(\frac{x_0}{2}\right) - \vartheta\left(-\frac{x_0}{2}\right)\right] + n_0, \end{aligned} \tag{3}$$

where $-eN$ gives the charge difference between the left and right leads, $-en$ is the total electronic charge occupying the dot, and n_0 describes a possible offset charge. Note that with our conventions, N decreases (increases) when electrons are transferred towards the right (left) lead. Likewise, n increases (decreases) for tunneling onto (out) of the dot. The Hamiltonian (1) has been studied in most of the previous works on the subject and also forms the basis of our work.

The linear conductance through the dot is periodic in $N_0 = ceV_G/E_s$, and we can restrict ourselves to one period, $0 \le N_0 \le 1$, where G has a resonance peak at $N_0 = 1/2$. One can compute G analytically for the non-interacting limit, $g = 1$, by refermionizing this model,[28]

$$\frac{G_{g=1}}{G_0} = \int \frac{dE}{4T\cosh^2(E/2T)} \frac{w^2}{\cos^2(\pi[N_0 + E/E_s]) + w^2}, \tag{4}$$

with $G_0 = e^2/h$ and $w = (4-\lambda^2)^2/[8\lambda(4+\lambda^2)]$, where $\lambda = \pi U_{\rm imp}/D$ for the bandwidth D, which provides a high-energy cut-off. For strong barriers, Eq. (4) leads to the standard Breit-Wigner resonant tunneling line shape with linewidth $\Gamma_0 = wE_s/\pi$. (For $g = 1$, the infinite-barrier limit is reached already for $\lambda = 2$, where the associated phase shift is in the unitary limit.) Unfortunately, as the model (1) is not integrable for $g < 1$, exact solutions covering a wide parameter range of interest for this transport problem are out of reach. Analytical progress then generally has to rely on approximations. Initial work[14,20,21] pursued perturbative approaches, using the renormalization group, instanton methods or cumulant expansions, both for strong and weak barriers. Furusaki[22] presented a detailed study of the *uncorrelated sequential tunneling* (UST) regime, including also cotunneling contributions important away from the resonance peak. This regime allows for a *master equation approach*, whose validity requires that the barriers are sufficiently strong and that the temperature T is sufficiently high. For T well above ε but still below E_c, the discrete nature of the plasmon modes on the dot is not relevant while Coulomb blockade still exists. Then the corresponding results of Ref. 14 apply. In particular, one obtains power-law scaling for the peak conductance with $\alpha = 2(1/g-1)$, implying that in this case the double barrier effectively acts as a single impurity. In what follows, we only discuss the case $T < \varepsilon$.

Keeping only rates to lowest order in Γ_0 from the TLL leads onto the island (dot), which is equivalent to taking the standard UST mechanism, the conductance is given by[22]

$$\frac{G_{\rm UST}}{G_0} = \frac{\Gamma_0(\pi T/D)^{-1+1/g}}{4\Gamma(1/g)T\cosh(\delta/2T)} \left|\Gamma\left(\frac{1}{2g} + \frac{i\delta}{2\pi T}\right)\right|^2, \tag{5}$$

where $\Gamma(x)$ denotes the Gamma function, and $\delta = E_c|N_0 - 1/2|$ measures the distance from the resonance peak. The hybridization $\Gamma_0 = 2\pi\rho_0\Delta^2$ can be expressed in terms of the 1D density of states, $\rho_0 = 1/(\pi v_F)$, and the hopping amplitude Δ onto the dot,[30]

$$\Delta = \pi^{-1}\Gamma(1+1/g)\Gamma^{1/g}(1+g)(\pi U_{\rm imp}/D)^{-1/g}D. \tag{6}$$

The line shape (5) is rather close to the Fermi-liquid form (4) for large barrier heights and evidently characterized by a linear T dependence of the linewidth. In the tails of a peak, the conductance (5) vanishes exponentially, but then also (elastic) cotunneling has to be included.[20,21,22] Note that the UST peak conductance in Eq. (5) scales as $G_{\rm max} \propto T^{-2+1/g}$, so that the power-law exponent is $\alpha_{\rm UST} = -2 + 1/g$. Finally, at low temperatures, instead of sequential tunneling, *coherent resonant tunneling* is possible, characterized by non-Lorentzian universal line shapes,[14] where the linewidth scales as T^{1-g}. In this paper, we only address the incoherent regime by employing a Markovian master equation approach. Moreover, we focus on the temperature dependence of the peak conductance, for which cotunneling is always a subleading process.[22] Therefore we neglect cotunneling throughout this work. This is not a fundamental restriction to our approach, but implies some technical simplifications. On resonance, the basically only restriction for the validity of our master equation approach is then given by the condition $G_{\rm max} \ll G_0$.[22]

Remarkably, the available experimental data obtained in SWNTs[15] seem incompatible with Eq. (5), since the observed temperature dependence of the conductance peak height $G_{\rm max}$ does not follow the UST scaling but rather suggests a $T^{-3+2/g}$ power law. The exponent $\alpha_{\rm CST} = -3 + 2/g$ has been proposed to arise from a "correlated sequential tunneling" (CST) mechanism.[24] CST processes are sequential tunneling processes that cannot be subdivided into two uncorrelated steps, yet still can be captured in a master equation framework. Such processes have been studied previously in the chemical physics community, e.g., in the context of electron

transfer reactions through an intermediate bridge state. In particular, Hu and Mukamel[31] have treated the sequential tunneling regime for this problem using a very similar master equation theory. Here we compute the sequential tunneling current through a double barrier in a TLL, see Eq. (1), beyond the lowest order in Γ_0, implying modifications to Eq. (5). We analyze to what extent such processes could indeed cause power-law scaling in $G_{\max}(T)$ with the CST exponent $\alpha_{\rm CST}$.

The remainder of the paper is structured as follows. In Sec. II we introduce the general master equation approach, and apply it to the regime of linear transport. The transition rates entering the master equation are evaluated in Sec. III, and in Sec. IV explicit results for the temperature dependence of the conductance peak, $G_{\max}(T)$, are presented. We conclude by discussing our results and their relation to other (experimental as well as theoretical) work in Sec. V. Technical details concerning Sec. III can been found in the Appendix.

II. MARKOVIAN MASTER EQUATION

Let us start with the case of large tunneling barriers $U_{\rm imp}$, which can be described within a dual version of Eq. (1), see Refs. 14,20,22,30. In this regime, the dynamics is dominated by tunneling events connecting minima of the periodic potential $H_{\rm imp} = 2U_{\rm imp}\cos(\pi N)\cos(\pi n)$ in the (N,n)-plane.[14] Such tunneling events induce a change $n \to n \pm 1$ for tunneling onto/out of the dot, and $N \to N \mp 1$ for tunneling towards the right/left. Hence transfer of one unit of charge across the complete double barrier structure requires $N \to N \pm 2$. The current through the double barrier is then given by

$$I = \frac{e}{2}\langle \dot{N}\rangle, \tag{7}$$

where the expectation value stands for a quantum-statistical average with Hamiltonian (1), and Eq. (7) has to be evaluated in the stationary long-time limit. The discrete dynamics underlying Eq. (7) can be described by a master equation[32] for the probability $P_N(n,t)$ of being in state (N,n) at time t.

Master equations have previously been employed for the non interacting case,[17,18,19] and for the TLL case to lowest order in Γ_0.[22,23] The rates entering the master equation can be extracted as irreducible diagrams for the self-energy,[30] which to lowest order are simple golden rule rates. These first-order UST contributions to the transition rates imply $N \to N \pm 1$ jumps. Below we will systematically take into account transition rates up to second order in Γ_0. It turns out that the second-order contributions to those rates are plagued by nontrivial divergences, which require a resummation of higher-order diagrams. This resummation is done below by employing the Weisskopf-Wigner approximation.[33] On the one hand, this procedure yields a direct CST process, $N \to N \pm 2$. On the other hand, additional (indirect) CST contributions to the transition rates for $N \to N \pm 1$ arise. Apart from the need of a regularization scheme, the same situation is encountered in the theory of bridged electron transfer reactions.[31]

The master equation for $P_N(n,t)$ then has the general structure[32]

$$\begin{aligned}\dot{P}_N(n,t) = &-\gamma(n)P_N(n,t) \\ &+\Gamma^f_R(n+1)P_{N+1}(n+1,t) + \Gamma^b_L(n+1)P_{N-1}(n+1,t) \\ &+\Gamma^f_L(n-1)P_{N+1}(n-1,t) + \Gamma^b_R(n-1)P_{N-1}(n-1,t) \\ &+\Gamma^f_{CST}(n)P_{N+2}(n,t) + \Gamma^b_{CST}(n)P_{N-2}(n,t) \\ &-\Gamma^f_{CST}(n)P_N(n,t) - \Gamma^b_{CST}(n)P_N(n,t),\end{aligned} \tag{8}$$

where $\Gamma^{f/b}_{L/R}(n)$ denotes the forward/backward rate for a transition over the left/right barrier, having *started* with n electrons on the dot. In addition, $\Gamma^{f/b}_{CST}(n)$ denotes the forward/backward rate for a direct CST transition $N \to N \pm 2$. Moreover, we use

$$\gamma(n) = \Gamma^f_R(n) + \Gamma^f_L(n) + \Gamma^b_R(n) + \Gamma^b_L(n), \tag{9}$$

which is related to the linewidth of the state (N,n). It is useful to also introduce the probability

$$p(n,t) = \sum_{N=-\infty}^{+\infty} P_N(n,t) \tag{10}$$

for the dot being occupied with n electrons at time t. In order to calculate the current I, we insert Eq. (8) into Eq. (7), which yields after some algebra

$$\begin{aligned} I \;=\; -\frac{e}{2}\sum_{n=-\infty}^{+\infty} &\Big[\Gamma^f_R(n) + \Gamma^f_L(n) - \Gamma^b_R(n) - \Gamma^b_L(n) \\ &+\; 2\Gamma^f_{CST}(n) - 2\Gamma^b_{CST}(n)\Big]p(n, t\to\infty).\end{aligned} \tag{11}$$

Summing both sides of Eq. (8) over N, we obtain a master equation for $p(n,t)$ directly,

$$\begin{aligned}\dot{p}(n,t) \;=\; &-\gamma(n)p(n,t) \\ &+\; \Big[\Gamma^b_L(n+1) + \Gamma^f_R(n+1)\Big]\,p(n+1,t) \\ &+\; \Big[\Gamma^f_L(n-1) + \Gamma^b_R(n-1)\Big]\,p(n-1,t).\end{aligned} \tag{12}$$

The stationary solution $p(n) = p(n, t\to\infty)$ follows by requiring $\dot{p}(n) = 0$, which yields the detailed balance relation

$$\frac{p(n)}{p(n+1)} = \frac{\Gamma^b_L(n+1) + \Gamma^f_R(n+1)}{\Gamma^f_L(n) + \Gamma^b_R(n)}. \tag{13}$$

Taking into account conservation of probability, $\sum_{n=-\infty}^{\infty} p(n) = 1$, this relation can be solved recursively. We note that the direct CST rates $\Gamma^{f/b}_{CST}(n)$ do not appear in Eq. (12), since they do not alter the net

population of the dot. However, they do appear in the current (11).

Let us now focus on the linear transport regime and sufficiently low temperatures, $eV, T \ll E_c$, where at most two charge states n are allowed on the dot due to charging effects.[19] Without loss of generality, we may choose $n = 0$ and $n = -1$ to label those states. In the linear transport regime, we can disregard the rates $\Gamma_L^f(0), \Gamma_R^f(-1), \Gamma_R^b(0)$, and $\Gamma_L^b(-1)$, since they involve energetically forbidden states with dot occupation numbers $n = +1$ or $n = -2$. The recursive solution of the detailed balance relation (13) then yields

$$p(0) = \frac{\Gamma_L^f(-1) + \Gamma_R^b(-1)}{\Gamma_L^b(0) + \Gamma_R^f(0) + \Gamma_L^f(-1) + \Gamma_R^b(-1)}, \quad (14)$$

$$p(-1) = \frac{\Gamma_L^b(0) + \Gamma_R^f(0)}{\Gamma_L^b(0) + \Gamma_R^f(0) + \Gamma_L^f(-1) + \Gamma_R^b(-1)}.$$

Combining Eqs. (14) and (11), we obtain $I = I_1 + I_2$, with the standard contribution[17,18,19,22,23]

$$I_1 = -e\frac{\Gamma_R^f(0)\Gamma_L^f(-1) - \Gamma_R^b(-1)\Gamma_L^b(0)}{\Gamma_R^f(0) + \Gamma_L^f(-1) + \Gamma_R^b(-1) + \Gamma_L^b(0)}, \quad (15)$$

and an additional term caused by direct CST rates,

$$I_2 = -e\frac{\left[\Gamma_{CST}^f(0) - \Gamma_{CST}^b(0)\right]\left[\Gamma_L^f(-1) + \Gamma_R^b(-1)\right] + \left[\Gamma_{CST}^f(-1) - \Gamma_{CST}^b(-1)\right]\left[\Gamma_L^b(0) + \Gamma_R^f(0)\right]}{\Gamma_R^f(0) + \Gamma_L^f(-1) + \Gamma_R^b(-1) + \Gamma_L^b(0)}. \quad (16)$$

So far we have discussed a general procedure to determine the current in the linear regime. To make progress, the transition rates entering the above equations must be computed for the Hamiltonian in Eq. (1).

III. TRANSITION RATES

We now systematically compute all rates entering Eqs. (15) and (16). Rates of order higher than Γ_0^2 will be included approximately within the Weisskopf-Wigner scheme. For consistency, besides the direct CST rates, it is also mandatory to include all indirect CST contributions to the rates $\Gamma_\lambda^\nu(n)$ with $\lambda = L/R$ and $\nu = f/b$. All these transition rates can be extracted as the irreducible components of an exact perturbation series expression for the probability distribution $P_N(n,t)$. The latter corresponds to the diagonal element of the reduced density matrix (RDM), which in turn allows for a path-integral representation.[30] Tracing out the Gaussian TLL modes away from the barriers at $x = \pm x_0/2$, one obtains an effective action which is equivalent to the action of a quantum Brownian particle hopping in the (N,n)-plane.[14,21] Then a path can be visualized in the (N,N')-plane of the RDM, see Fig. 1, with a corresponding dynamics in the (n,n')-plane. Alternatively, the rate expressions given below can also be derived using the projection operator formalism.[31,32,34] The rates $\Gamma_\lambda^\nu(n)$ for a transition $N \to N \pm 1$ then have contributions of first and at least second order in Γ_0,

$$\Gamma_\lambda^\nu(n) = \Gamma_\lambda^{\nu,(1)}(n) + \Gamma_\lambda^{\nu,(2)}(n), \quad (17)$$

where we keep only the $n = 0, -1$ states.

A. First-order rates

The first-order contribution is well-known,[14,20,21,22,30] and schematically depicted in Fig. 2(a). There are two independent (uncorrelated) steps, one from the left TLL "lead" onto the island, and another to the right TLL "lead". Using the hopping matrix element Δ in Eq. (6), these steps individually correspond to irreducible golden rule rates,

$$\Gamma_\lambda^{\nu,(1)}(n) = \frac{\Delta^2}{2}\mathrm{Re}\int_0^\infty dt \exp[iE_{\lambda\nu}(n)t - W_\Sigma(t)], \quad (18)$$

where $W_\Sigma(t) = W_+(t) + W_-(t)$, with the correlation functions[21]

$$W_\pm(t) = \int_0^\infty d\omega \frac{J_\pm(\omega)}{\omega^2}\{[1 - \cos(\omega t)] \times \coth(\omega/2T) + i\sin(\omega t)\}. \quad (19)$$

The spectral densities follow as

$$J_\pm(\omega) = \frac{\omega e^{-\omega/D}}{2g}\left[1 + 2\varepsilon\sum_{m=1}^\infty \delta(\omega - \mathcal{M}_\pm(m)\varepsilon)\right], \quad (20)$$

where $\mathcal{M}_+(m) = 2m-1$, $\mathcal{M}_-(m) = 2m$, and $\varepsilon = E_s/g = \pi v_F/(g x_0)$ is the plasmon level spacing on the dot. The δ-peaks are a result of the finite level spacing on the dot, while the first part in Eq. (20) yields a standard Ohmic spectral density. The bandwidth D is taken as smooth (exponential) ultraviolet cutoff for the model (1). These correlation functions arise in the process of integrating out the TLL modes away from the barrier, see Ref. 30 for a detailed review of this procedure. Finally, the energies $E_{\lambda,\nu}(n)$ appearing in Eq. (18) are defined as

$$\begin{aligned} E_{Rf}(n+1) &= -E_{Rb}(n) = \mu(n+1) - eV/2, \\ E_{Lb}(n+1) &= -E_{Lf}(n) = \mu(n+1) + eV/2, \end{aligned} \quad (21)$$

with the electrochemical potential

$$\mu(n+1) = 2E_c(n - n_0 - ecV_G/2E_c + 1/2).$$

The correlation function $W_\Sigma(t) = W_+ + W_- = W_{\rm Ohm} + W_{\rm dot}$ can be decomposed into two different parts,[21,23] namely an Ohmic part $W_{\rm Ohm}(t)$ and an oscillatory part $W_{\rm dot}(t)$. Here the first contribution comes from the smooth part in $J_\pm(\omega)$, and takes the standard form

$$\begin{aligned} W_{\rm Ohm}(t) &= \frac{1}{g}\ln[(D/T)\sinh|\pi T t|] + i(\pi/g)\mathrm{sgn}(t) \\ &= S_{\rm Ohm}(t) + iR_{\rm Ohm}(t). \end{aligned} \quad (22)$$

At low temperatures, $T \ll \varepsilon$, the dot correlation function is given by its $T = 0$ limiting form

$$W_{\rm dot}(t) = \frac{1}{g}\ln\left(\frac{1 - e^{-(\varepsilon/D + i\varepsilon t)}}{1 - e^{-\varepsilon/D}}\right), \quad (23)$$

up to exponentially small corrections in $y = e^{-\varepsilon/T}$. This function arises due to the finite level spacing, and is periodic in t with period $\tau_\varepsilon = 2\pi/\varepsilon$. It can therefore be expanded in a Fourier series,[23] leading to

$$\Gamma_\lambda^{\nu,(1)}(n) = \sum_{p=-\infty}^{+\infty} d_p(\varepsilon)\, \Gamma_{\rm Ohm}(E_{\lambda\nu}(n) - p\varepsilon). \quad (24)$$

The Fourier coefficients $d_p(\varepsilon)$ can be found in the Appendix, and from Eq. (22), one gets[30]

$$\Gamma_{\rm Ohm}(E) = \frac{\Delta^2}{4D}\frac{e^{E/2T}}{\Gamma(1/g)}\left(\frac{D}{2\pi T}\right)^{1-1/g}\left|\Gamma\left(\frac{1}{2g} + \frac{iE}{2\pi T}\right)\right|^2, \quad (25)$$

which in turn directly leads to Eq. (5). We note that the first-order forward/backward rates (18) fulfill a detailed balance relation

$$\Gamma_\lambda^{b,(1)}(n-1) = e^{-E_{\lambda f}(n)/T}\Gamma_\lambda^{f,(1)}(n), \quad (26)$$

which formally follows from the reflection property $W_\pm(-t) = W_\pm^*(t) = W_\pm(t - i/T)$ of the above correlation functions.

k	Indirect transitions $N \to N-1$:
1	$N, N \to a \to N, N \to b \to N-1, N-1$
2	$N, N \to a \to N, N \to b' \to N-1, N-1$
3	$N, N \to b \to N, N \to b \to N-1, N-1$
4	$N, N \to b \to N, N \to b' \to N-1, N-1$
5	$N, N \to b \to N-1, N-1 \to b \to N-1, N-1$
6	$N, N \to b \to N-1, N-1 \to b' \to N-1, N-1$
7	$N, N \to b \to N-1, N-1 \to c \to N-1, N-1$
8	$N, N \to b \to N-1, N-1 \to c' \to N-1, N-1$
#	Direct transitions $N \to N-2$:
CST1	$N, N \to b \to N-1, N-1 \to c \to N-2, N-2$
CST2	$N, N \to b \to N-1, N-1 \to c' \to N-2, N-2$

TABLE I: All transition processes of order Γ_0^2 contributing to the master equation. The off-diagonal states a, b and c are specified in Fig. 1.

B. Indirect CST rates

The Γ_0^2 contributions to the rate for $N \to N-1$, which we shall call "indirect transitions", require a careful counting of all possible transitions consisting of four jumps in the (N, N')-plane, see Figure 1 and Table I. There are eight irreducible diagrams for the forward rate, plus their complex conjugates, which can however be included by taking twice the real part. Similarly, there are eight diagrams for the backward rate. Each irreducible second-order diagram then gives a triple integral over three times τ_1, τ_2 and τ_3, which represent the time spent in the corresponding state of the reduced density matrix (RDM).[21,30] To give a concrete example, the diagram denoted by $k = 7$ in Table I is drawn schematically in Fig. 3(a). In particular, since we neglect cotunneling processes, after two jumps we are always in a diagonal state of the RDM, amounting to a real (as opposed to virtual) occupation of the corresponding state. Therefore τ_2 in those expressions will always have the meaning of the time spent in the respective intermediate diagonal state. Similarly, for the "direct" CST rate with $N \to N-2$, there are two such triple-integral contributions (plus their complex conjugate diagrams). At this point, we note that we label the direct transitions as CST1/2 and the indirect transitions with the index $k = 1, \ldots, 8$, although in principle *all* second-order processes taken into account here are correlated sequential tunneling processes.

An important property of the irreducible second-order diagrams is that for finite plasmon level spacing ε, each of them contains a divergence. This is not a trivial divergence as we work with irreducible diagrams. Formally, this infrared divergence comes from the τ_2 integration that extends from 0 to ∞ but has an integrand which is ultimately periodic in τ_2. This implies that one has to effectively include higher-order diagrams, which is of course impossible to achieve in an exact way. Here we use the Weisskopf-Wigner approximation[33] to regularize the second-order diagrams. Physically, the intermediate state has a finite lifetime linked to the linewidth param-

eter $\gamma(n)$ in Eq. (9). We then introduce a factor $e^{-\gamma(n)\tau_2}$ for the τ_2-integrations, where the linewidth $\gamma(n)$ has to be computed self-consistently by requiring that Eq. (9) holds. This linewidth $\gamma(n)$ then enters the master equations (8) and (12).

The eight regularized rates $\Gamma^{\nu,(2)}_{\lambda,k}$ are given explicitly in Table II. At low temperatures, again the $T = 0$ form

$$W_\Delta(t) = W_+(t) - W_-(t) = -\frac{1}{g}\ln\left(\frac{1+e^{-(\varepsilon/D+i\varepsilon t)}}{1+e^{-\varepsilon/D}}\right) \tag{27}$$

holds up to exponentially small corrections of order $y = e^{-\varepsilon/T}$, and

$$\Gamma^{\nu,(2)}_\lambda = \sum_{k=1}^{8}\Gamma^{\nu,(2)}_{\lambda,k}. \tag{28}$$

This rate depends on $\gamma(n)$, which needs to be determined self-consistently. Note that $W_\Delta(t)$ is also periodic in t with period τ_ε.

From now on, we always focus on the resonance peak, where all energies can be put to $E_{\lambda\nu}(n) = 0$. In addition, since on resonance $\mu(-1) = \mu(0)$, we also have $\gamma(-1) = \gamma(0) = \gamma$. The calculation of $\Gamma^{\nu,(2)}_{\lambda,k}$ is comparatively simple for the diagrams $k = 1, 2, 7, 8$, since only the periodic correlation function W_Δ appears in the respective bracketed terms, which allows for a Fourier series expansion. Then the triple integrals factorize, and the quickly converging Fourier sums can easily be performed numerically. For the benefit of the interested reader, in order to illustrate this procedure, the evaluation of diagrams of this first class is discussed in full detail in the Appendix. The remaining diagrams of the second class ($k = 3, 4, 5, 6$) are more difficult to handle, since the bracketed terms now involve the correlation function W_Σ. We have therefore evaluated the respective triple integrals numerically as a function of the linewidth γ. This can be done either via direct numerical quadrature (trapezoidal rule), or using Monte Carlo integration[35]. The latter approach is more suitable for large γ, where stochastic error bars can be made arbitrarily small with only modest computational effort. Fortunately, the γ-dependence of the four diagrams of the second class ($k = 3, 4, 5, 6$) turns out to be identical to the one of the first class, which is given by Eq. (29) below, see also Eq. (A3) in the Appendix. A fit of the numerical results for several γ then allows to accurately extract the parameters $A_{g,k}, B_{g,k}$ and $C_{g,k}$ for those diagrams as well. Finally, we summarize *all indirect CST contributions* as

$$\Gamma^{\nu,(2)}_\lambda = \frac{\Delta^4}{\varepsilon^3}\left(-\frac{\varepsilon}{\gamma}A_g + \frac{\gamma}{\varepsilon}B_g + C_g\right), \tag{29}$$

where dimensionless parameters A_g, B_g, and C_g follow by summing over the respective values $A_{g,k}, B_{g,k}, C_{g,k}$ for these eight diagrams (including their complex conjugates), see Appendix A. These parameters depend on the TLL parameter g and on the dimensionless temperature T/ε.

Of primary interest is then the temperature dependence of the self-consistently determined linewidth parameter γ. Unfortunately, as we discussed above, it seems impossible to evaluate A_g, B_g, and C_g analytically, even in the non-interacting limit $g = 1$. However, numerically we can obtain them for given (g, T), see Appendix A for details, and we find $B_g \approx A_g < C_g$. Since the master equation approach holds only for $\gamma \ll \varepsilon$, it is clear that the B_g term in Eq. (29) can be neglected for all practical purposes. Numerical results for A_g and C_g for different g and T are shown in Table III and Fig. 4, respectively. Equation (29) indicates that C_g follows from the large-γ behavior of $\Gamma^{\nu,(2)}_\lambda$, while determining A_g requires the small-γ solution of the relevant triple integral. Unfortunately, the latter is numerically rather expensive at low temperatures, and hence we can specify A_g only for moderately low T, see Table III, while Fig. 4 covers our results for C_g down to $T = 0.01\varepsilon$. Evidently, the temperature dependence of C_g becomes rather weak at low temperatures, $C_g(T) \simeq$ const., an observation supported by analytical arguments given in Appendix A. Based on these arguments, we expect that even for $g = 0.9$, where Fig. 4 suggests a significant T-dependence, at sufficiently low T the quantity C_g becomes independent of temperature.

We mention in passing that in contrast to the first-order contributions in Sec. III A, the above indirect CST contributions do not obey detailed balance. This is true although the correlation functions entering these rates in Table II still have the reflection property. The violation of the detailed balance relation follows directly by inspection of the triple integrals in Table II, i.e., forward and backward rates are not linked by a relation of the form (26). Of course, the total rates and populations of the states are still linked by detailed balance, but there is no reason why individual rates should obey Eq. (26). A simple example for this fact is given by superexchange rates in electron transfer theory,[30,31] see also Ref. 36 for related observations.

C. Direct CST rates

The direct CST rates $\Gamma^\nu_{CST}(n)$ for a transition $N \to N-2$ have only contributions of at least order Γ_0^2. There are two possible transition processes CST1 and CST2, see Table I and Figs. 1 and 3(b). The corresponding transition rates are simply

$$\Gamma^f_{CST,1}(n) = -\Gamma^{f,(2)}_{R,7}(n), \quad \Gamma^f_{CST,2}(n) = -\Gamma^{f,(2)}_{R,8}(n). \tag{30}$$

These relations hold not only on resonance but in general. Since CST transitions do not alter the stationary population $p(n)$, they do not enter the linewidth (9). The rates $\Gamma^\nu_{CST}(n)$ *per se* are also not subject to a detailed balance relation (26). Note that the cotunneling diagram

Forward $N \to N-1$ rates of (at least) order Γ_0^2 over the right barrier:

$$\Gamma^{f,(2)}_{R,1}(n) = -2\tfrac{\Delta^4}{16}\mathrm{Re}\int_0^\infty d\tau_i \times e^{i[-E_{Lb}(n)\tau_1+E_{Rf}(n)\tau_3]}e^{-W^*_\Sigma(\tau_1)-W_\Sigma(\tau_3)}\left[e^{W^*_\Delta(\tau_1+\tau_2)-W^*_\Delta(\tau_2)-W^*_\Delta(\tau_1+\tau_2+\tau_3)+W^*_\Delta(\tau_2+\tau_3)}-1\right]e^{-\gamma(n)\tau_2}$$

$$\Gamma^{f,(2)}_{R,2}(n) = -2\tfrac{\Delta^4}{16}\mathrm{Re}\int_0^\infty d\tau_i \times e^{i[-E_{Lb}(n)\tau_1-E_{Rf}(n)\tau_3]}e^{-W^*_\Sigma(\tau_1)-W^*_\Sigma(\tau_3)}\left[e^{-W^*_\Delta(\tau_1+\tau_2)+W^*_\Delta(\tau_2)+W^*_\Delta(\tau_1+\tau_2+\tau_3)-W^*_\Delta(\tau_2+\tau_3)}-1\right]e^{-\gamma(n)\tau_2}$$

$$\Gamma^{f,(2)}_{R,3}(n) = -2\tfrac{\Delta^4}{16}\mathrm{Re}\int_0^\infty d\tau_i \times e^{i[E_{Rf}(n)\tau_1+E_{Rf}(n)\tau_3]}e^{-W_\Sigma(\tau_1)-W_\Sigma(\tau_3)}\left[e^{W_\Sigma(\tau_1+\tau_2)-W_\Sigma(\tau_2)-W_\Sigma(\tau_1+\tau_2+\tau_3)+W_\Sigma(\tau_2+\tau_3)}-1\right]e^{-\gamma(n)\tau_2}$$

$$\Gamma^{f,(2)}_{R,4}(n) = -2\tfrac{\Delta^4}{16}\mathrm{Re}\int_0^\infty d\tau_i \times e^{i[E_{Rf}(n)\tau_1-E_{Rf}(n)\tau_3]}e^{-W_\Sigma(\tau_1)-W^*_\Sigma(\tau_3)}\left[e^{-W_\Sigma(\tau_1+\tau_2)+W_\Sigma(\tau_2)+W_\Sigma(\tau_1+\tau_2+\tau_3)-W_\Sigma(\tau_2+\tau_3)}-1\right]e^{-\gamma(n)\tau_2}$$

$$\Gamma^{f,(2)}_{R,5}(n) = -2\tfrac{\Delta^4}{16}\mathrm{Re}\int_0^\infty d\tau_i \times e^{i[E_{Rf}(n)\tau_1-E_{Rb}(n-1)\tau_3]}e^{-W_\Sigma(\tau_1)-W^*_\Sigma(\tau_3)}\left[e^{W_\Sigma(\tau_1+\tau_2)-W^*_\Sigma(\tau_2)-W_\Sigma(\tau_1+\tau_2+\tau_3)+W^*_\Sigma(\tau_2+\tau_3)}-1\right]e^{-\gamma(n)\tau_2}$$

$$\Gamma^{f,(2)}_{R,6}(n) = -2\tfrac{\Delta^4}{16}\mathrm{Re}\int_0^\infty d\tau_i \times e^{i[E_{Rf}(n)\tau_1+E_{Rb}(n-1)\tau_3]}e^{-W_\Sigma(\tau_1)-W_\Sigma(\tau_3)}\left[e^{-W_\Sigma(\tau_1+\tau_2)+W^*_\Sigma(\tau_2)+W_\Sigma(\tau_1+\tau_2+\tau_3)-W^*_\Sigma(\tau_2+\tau_3)}-1\right]e^{-\gamma(n)\tau_2}$$

$$\Gamma^{f,(2)}_{R,7}(n) = -2\tfrac{\Delta^4}{16}\mathrm{Re}\int_0^\infty d\tau_i \times e^{i[E_{Rf}(n)\tau_1+E_{Lf}(n-1)\tau_3]}e^{-W_\Sigma(\tau_1)-W_\Sigma(\tau_3)}\left[e^{W_\Delta(\tau_1+\tau_2)-W^*_\Delta(\tau_2)-W_\Delta(\tau_1+\tau_2+\tau_3)+W^*_\Delta(\tau_2+\tau_3)}-1\right]e^{-\gamma(n)\tau_2}$$

$$\Gamma^{f,(2)}_{R,8}(n) = -2\tfrac{\Delta^4}{16}\mathrm{Re}\int_0^\infty d\tau_i \times e^{i[E_{Rf}(n)\tau_1-E_{Lf}(n-1)\tau_3]}e^{-W_\Sigma(\tau_1)-W^*_\Sigma(\tau_3)}\left[e^{-W_\Delta(\tau_1+\tau_2)+W^*_\Delta(\tau_2)+W_\Delta(\tau_1+\tau_2+\tau_3)-W^*_\Delta(\tau_2+\tau_3)}-1\right]e^{-\gamma(n)\tau_2}$$

TABLE II: The 8 irreducible rate expressions of at least order Γ_0^2, corresponding to the forward-rate diagrams through the right barrier, $\Gamma^{f,(2)}_{R,k}$, see Eq. (28) and Table I. The corresponding rates through the left barrier, $\Gamma^{f,(2)}_{L,i}(n-1)$, follow by substituting $E_{Rf/Lb}(n) \to E_{Lf/Rb}(n-1)$ and $E_{Lf/Rb}(n-1) \to E_{Rf/Lb}(n)$. The backward rates $\Gamma^{b,(2)}_{R,i}(n-1)$ and $\Gamma^{b,(2)}_{L,i}(n)$ can be obtained from the forward rates $\Gamma^{f,(2)}_{R,i}(n)$ and $\Gamma^{f,(2)}_{L,i}(n-1)$ using the substitutions $E_{Lb/Rf}(n) \to E_{Lf/Rb}(n-1)$ and $E_{Lf/Rb}(n-1) \to E_{Lb/Rf}(n)$, respectively.

	$T = 0.1\varepsilon$	$T = 0.2\varepsilon$	$T = 0.5\varepsilon$
$g = 0.4$	3.37×10^{-8}	-1.56×10^{-8}	-1.12×10^{-8}
$g = 0.5$	3.00×10^{-8}	-2.02×10^{-8}	-6.07×10^{-8}
$g = 0.6$	2.35×10^{-8}	9.71×10^{-9}	2.83×10^{-7}
$g = 0.7$	-1.97×10^{-8}	2.32×10^{-8}	1.34×10^{-6}
$g = 0.8$	-1.42×10^{-7}	7.68×10^{-8}	3.86×10^{-6}
$g = 0.9$	-3.76×10^{-7}	7.35×10^{-7}	7.85×10^{-6}

TABLE III: Numerical results for the dimensionless parameter A_g in Eq. (29) for various g and T at $D = 10\varepsilon$.

in Fig. 2(b) is subleading on resonance and therefore not taken into account here.

D. Linewidth

On resonance, $E_{\lambda\nu}(n) = 0$, and hence forward and backward rates are equal,

$$\Gamma^{f,(1)/(2)}_\lambda = \Gamma^{b,(1)/(2)}_\lambda \equiv \Gamma^{(1)/(2)}. \tag{31}$$

Neglecting the B_g-term as explained above, the self-consistency equation for γ can then be written as

$$\gamma = 4(\Gamma^{(1)} + \Gamma^{(2)}) = 4\Gamma^{(1)} + \frac{4\Delta^4}{\varepsilon^3}\left(-\frac{\varepsilon}{\gamma}A_g + C_g\right). \tag{32}$$

This quadratic equation has two real solutions, as long as the dimensionless parameter $\xi < 1$, where

$$\xi = \frac{\Delta^4\varepsilon^4 A_g}{(\varepsilon^3\Gamma^{(1)} + \Delta^4 C_g)^2}. \tag{33}$$

If indeed $\xi < 1$, these solutions are given by

$$\gamma_\pm = 4\left[\Gamma^{(1)} + \frac{\Delta^4 C_g}{\varepsilon^3}\right]\frac{1 \pm \sqrt{1-\xi}}{2}. \tag{34}$$

For $\xi \ll 1$, we thus have

$$\gamma \equiv \gamma_+ \approx 4\left(\Gamma^{(1)} + \frac{\Delta^4 C_g}{\varepsilon^3}\right), \tag{35}$$

and $\gamma_- = \xi\gamma_+/4$. For $\xi > 1$, the two solutions are complex valued, and γ acquires an imaginary part. If this happens, the description in terms of the master equation in combination with the Weisskopf-Wigner approximation is questionable and not used below. We identify the linewidth with the solution γ_+, since we recover the well-known result[20] $\gamma = 4\Gamma^{(1)}$ when second-order rates are neglected, while then $\gamma_- = 0$. The requirement $\xi < 1$ typically results in a temperature T_l determined by

$$\Delta^4 \frac{A_g(T_l)}{\varepsilon^2} = \left(\Gamma^{(1)}(T_l) + \frac{\Delta^4 C_g}{\varepsilon^3}\right)^2,$$

below which our Weisskopf-Wigner theory becomes problematic. This equation yields T_l provided $A_g(T)$ and C_g (assumed independent of temperature) are known. However, since no reliable low-T estimates for A_g are available, see Table III, it is often difficult to provide good estimates for T_l. Of course, the validity of the master equation in addition always requires $G_{\max} \ll G_0$. In what follows, the parameter C_g is assumed to be temperature independent and given by its value at $T/\varepsilon = 0.01$ in Fig. 4. Although we expect $C_g(T)$ to be constant (see above), we cannot rule out that this is approximative.

The linewidth $\gamma(T)$ now consists of two contributions. The first term in Eq. (35) is $\propto T^{1/g-1}$, while the second term is constant due to the T independence of C_g. This implies a crossover from power-law scaling of $\gamma(T)$ to a basically constant γ as the temperature is lowered. This crossover depends in an essential way on the tunneling amplitude Δ. Results for $\gamma(T)$ from Eq. (35) are shown in Fig. 5(a), taking $\Delta = 6\varepsilon$ and $D = 10\varepsilon$. Figure 5(b) shows (for several T) that the validity condition $\xi < 1$, with ξ defined in Eq. (33), is indeed fulfilled. This choice for Δ reflects rather transparent barriers, where CST effects are clearly pronounced. Obviously, at low T, Fig. 5 suggests that γ is essentially independent of temperature. This behavior is most pronounced for strong interactions (small g). Going towards less transparent barriers, $\gamma(T)$ is shown in Fig. 6 for $\Delta = 3\varepsilon$. In Sec. V, we argue that the hopping amplitudes Δ appropriate for the experiment in Ref. 15 and for the numerical simulations in Ref. 28 are comparable to this value. Now a crossover from the UST power law at high temperatures to an approximately T-independent behavior at low T becomes apparent. For $g \leq 1/2$, we now find $\xi > 1$, implying that our approach breaks down for such interactions. Finally, for very high barriers, $\Delta \to 0$, the linewidth is *always* dominated by the UST term, in accordance with standard reasoning.[22] This is illustrated in Fig. 7, where results for γ at $\Delta = 0.1\varepsilon$ are depicted. In this regime, higher-order corrections are obviously negligible.

Remarkably, for weak interactions, the linewidth γ is always dominated by the UST result over the *entire* range of temperatures where the master equation approach is valid ($\xi < 1$). CST effects then apparently do not have a finite domain of observability in the limit of weak interactions. We can therefore rationalize that previous calculations that essentially expand around the noninteracting case[25,26,29] do not observe a clear CST power-law scaling. The fate of CST effects near the noninteracting limit $g = 1$ will be further discussed at the end of Sec. IV. We conclude that *for CST effects to be observable, it is essential to allow for rather transparent barriers, a finite level spacing, and intermediate-to-strong interactions.* The parameter regime where CST plays a role is therefore rather narrow.

IV. TEMPERATURE DEPENDENCE OF CONDUCTANCE PEAK

The linear conductance G follows directly from Eqs. (15) and (16) by performing the derivative with respect to the transport voltage V. Moreover, since we are interested in the conductance maximum at resonance, we can put $\mu(n) = \mu(n+1) = 0$. For the first-order rates, the detailed balance relation (26) can be exploited. For the second-order rates, we find the relation $d\Gamma^{f,(2)}/dV = -d\Gamma^{b,(2)}/dV$. Finally setting $V = 0$, we obtain

$$G_{\max}(T) = G_{\max,A} + G_{\max,B}, \tag{36}$$

where

$$\begin{aligned} G_{\max,A} &= \frac{e^2}{T\gamma}\left(\Gamma^{(1)}\right)^2, \\ G_{\max,B} &= -e\Gamma^{(2)\prime} - 2e\Gamma'_{CST} + \frac{e^2}{T\gamma}\Gamma^{(1)}\Gamma^{(2)}. \end{aligned} \tag{37}$$

Here the prime denotes the derivative d/dV, taken at $V = 0$, and we omit the arguments of the rates, since on resonance they are all equal. The dominant term is the first term in $G_{\max,A}$. In order to show that the second term $G_{\max,B}$ is always negligible against $G_{\max,A}$, it is instructive to evaluate the second class of diagrams ($k = 3,4,5,6$) in Table II within a simple approximation. Since at long times the Ohmic part in $W_\Sigma(t)$ cancels out in the square-bracketed terms of the corresponding rate expressions in Table II, one may replace $W_\Sigma(t)$ by $W_{\rm dot}(t)$ in those square brackets. After this replacement, the Fourier expansion method discussed in the Appendix applies to all eight diagrams, with Fourier sums including terms like $dK_{\rm R/L}(E)/dE$. These sums can easily be calculated numerically. For all cases that are described below (and many more not shown here), we find that $G_{\max,B}$ is numerically zero. Although it looks like the

direct CST rates Γ_{CST} have effectively no influence in the end, this is not true since they exactly cancel certain contributions to the conductance coming from the indirect rate $\Gamma^{(2)}$. In that sense, the direct CST diagram, jumping by two steps along the diagonal of the reduced density matrix via an intermediate diagonal state, see Fig. 1, but without cutting the diagram in the intermediate state, is crucial for CST effects in the conductance maximum $G_{\max}$. Such diagrams are known to cause important effects in other systems,[31] but were previously not taken into account since the main focus was on the limit $\Delta \to 0$.

Hence we find for the conductance maximum

$$G_{\max}(T) \simeq \frac{e^2}{T\gamma}\left(\Gamma^{(1)}\right)^2. \tag{38}$$

Judging from our numerical results for $G_{\max,\mathrm{B}}$, the '$\simeq$' should in fact be replaced by an exact equality, although we have no analytical proof for this statement. For $T > T_c$, we find $\gamma \propto T^{1/g-1}$, leading to the UST result (5). However, for $T \lesssim T_c$, $\gamma(T)$ stays approximately constant, and hence an approximate power-law behavior follows,

$$G_{\max} \propto T^{2/g-3}, \tag{39}$$

with the CST exponent $\alpha_{\mathrm{CST}} = -3+2/g$. We stress that Eq. (39) is not meant in the sense of universal power-law scaling behavior. The crossover between UST and CST-dominated regimes occurs around a temperature T_c discussed below. The effective doubling in the exponent reflects the physics of this correlated transport process. For $T \ll \varepsilon$, plasmon modes excited on the island will correlate electrons in both leads. Since each lead has a end-tunneling density of states $\propto E^{1/g-1}$, correlated transport leads to an effective doubling in the exponent due to the presence of two leads.[24] Results for $G_{\max}(T)$ at $\Delta = 3\varepsilon$ are shown in Fig. 8 and follow Eq. (39) at low T. For $g \gtrsim 0.8$, the master equation breaks down ($G_{\max}$ exceeds G_0), while for $g \leq 1/2$, the validity condition $\xi < 1$ is violated. Nevertheless, there is a well-defined region of applicability, where CST effects are important and observable. Finally, for $\Delta = 0.1\varepsilon$, the expected UST scaling is recovered, see the inset of Fig. 8.

The crossover between the UST and CST regimes is characterized by a temperature $T_c = T_c(\Delta, g)$, which in turn follows from the condition that both contributions to γ in Eq. (35) be equal, $\Gamma^{(1)}(T_c) = \Delta^4 C_g/\varepsilon^3$. Although $\Gamma^{(1)}$ contains the sum over all Fourier modes, see Eq. (24), the zero mode $p = 0$ dominates on resonance, implying the condition $d_0\Gamma_{\mathrm{Ohm}}(0) = \Delta^4 C_g/\varepsilon^3$. This leads to the crossover temperature

$$T_c = \left(\frac{\Delta^2 C_g}{\eta_g \varepsilon^3}\right)^{g/(1-g)}, \tag{40}$$

where we use the abbreviation

$$\eta_g = \frac{(1-e^{-\varepsilon/D})^{1/g}\Gamma^2(1/2g)}{4D\Gamma(1/g)}(2\pi/D)^{1/g-1}.$$

In Fig. 9, results for the crossover temperature T_c are shown as a function of Δ/ε for the TLL parameters $g = 0.6$ and $g = 0.7$, always respecting the validity conditions $\xi(T_c) < 1$ and $G_{\max}(T_c) \ll G_0$. Generally, T_c increases when increasing Δ and/or decreasing g, i.e., for more transparent barriers and/or stronger interactions. Apparently, for weak interactions, $g \lesssim 1$, the Δ dependence of T_c becomes very steep, restricting the CST regime to extremely low temperatures for reasonable Δ. In practice, at such low temperatures coherent resonant tunneling processes dominate, rendering CST effects unobservable. For stronger interactions, however, CST effects can be pronounced even for moderately transparent barriers at low temperatures.

V. DISCUSSION

By using a master equation approach, linear transport in a TLL with two tunneling barriers forming a quantum dot has been studied. We find an approximate power-law temperature dependence of the peak conductance in the linear transport regime, with a characteristic g-dependent exponent, where g is the TLL parameter. By including second-order contributions to the tunneling rates in combination with a self-consistent Weisskopf-Wigner regularization, a comprehensive picture has been obtained. For temperatures below the plasmon level spacing $\varepsilon = \pi v_F/(g x_0)$ for dot size x_0, the dominant transport mechanism depends on the transparency Δ of the barriers. For sufficiently transparent barriers, $\Delta \gtrsim \varepsilon$, we find that correlated sequential tunneling (CST) is important, leading to an approximate power law with exponent $\alpha_{\mathrm{CST}} = -3 + 2/g$, while for very high barriers ($\Delta \to 0$), the uncorrelated sequential tunneling (UST) exponent $\alpha_{\mathrm{UST}} = -2 + 1/g$ is recovered. Note that despite the large Δ necessary to reach the CST regime, the master equation should still apply as the peak conductance remains small. We have determined the crossover temperature T_c separating both regimes. As a function of the physical parameters $(g, T, \Delta, \varepsilon, D)$, it is given by Eq. (40), where the dimensionless number C_g can be read off from Fig. 4. For $T < T_c$, the CST mechanism is effective, while for $T > T_c$, the UST picture is recovered. The peak conductance in the CST regime has been derived and is given by Eq. (38), with the well-known first-order rates $\Gamma^{(1)}$ specified in Eq. (24). The linewidth parameter γ as a function of the physical parameters is given in Eq. (35). These relations allow for a comparison to existing work and provide estimates for the parameter regime where such effects should be of importance. Notice that the modification of the standard picture of sequential tunneling here arises due to a renormalization of γ by higher-order processes, and we have given a physical explanation for this mechanism above.

Our findings regarding approximate CST power laws in $G_{\max}(T)$ are consistent with recent numerically exact real-time quantum Monte Carlo simulations[28] and also

with experimental observations. Let us first discuss the experimental work on SWNTs,[15] where the conductance through the dot followed the CST power law (39). From the exponent, the interaction strength was deduced to be $g = 0.54$, corresponding to a TLL parameter $g_\rho = 0.23$ for the charged sector of the effective four-channel TLL theory of SWNTs.[8,9] The quantum dot was formed by two nearby buckles acting as tunneling barriers. Since CST effects are predicted only for quite transparent barriers, it is instructive to estimate Δ. This is simpler for a single buckle used in earlier experiments,[11] where also a power-law linear conductance $G_{1B}(T)$ was observed. The single-barrier case is analytically solvable,[14] and for a high barrier,

$$\frac{G_{1B}}{4G_0} = \frac{\pi^{5/2}\Gamma(1+1/g)}{2\Gamma(1/2+1/g)}(\Delta/D)^2(\pi T/D)^{2/g-2}.$$

The measurements[11] for G_{1B} yield together with $g = 0.54$ a barrier transparency $\Delta \approx 45$ meV, taking a bandwidth of $D = 0.5$ eV; see Ref. 7. Assuming that the buckles have similar features when two are designed in a row, we can now establish a connection to the double-barrier case. In Ref. 15, $\varepsilon = 38$ meV was measured, yielding $\Delta \approx 1.2\varepsilon$, consistent with our conclusions above. For CST to be operative, one needs finite level spacing, low (but not too low) temperatures, and not too high barriers. These conditions apparently were met in the SWNT experiments in Ref. 15. Let us then comment on the Monte Carlo results of Ref. 28, where also the CST power law (39) has been found. For a direct comparison, we determine Δ for the potential strength $U_{\rm imp}$ used in Fig. 4 of Ref. 28. Using Eq. (6), for the simulation parameters $g = 0.6, U_{\rm imp} = 0.2D$, and $E_s = \pi D/20$, we find $\Delta \simeq 3.3\varepsilon$, again consistent with our conclusions. We note in passing that Eq. (39) has been obtained in Ref. 24 starting from finite-range interactions among the electrons. The divergence has been regularized by summing up a selection of higher-order terms. However, this selection was too strict,[37] leading to the incorrect conclusion that finite-range interactions would be a prerequisite for CST to occur. As shown here, also zero-range interactions suffice, as long as the tunneling barriers are not too high.

We emphasize that for Fermi liquid leads ($g = 1$) and $T \ll \varepsilon$, one finds $G_{\max} \propto T^{-1}$ both within a UST and a CST analysis. Several researchers recently approached the double-barrier TLL problem by considering weak interactions, g close to 1, without evidence for CST scaling.[25,26,29] As we have discussed in Sec. IV, in this weak-interaction limit, the crossover temperature T_c very quickly goes to zero when decreasing Δ, excluding CST effects for weak interactions even for finite level spacing. Put differently, for g close to 1, the master equation approach for large Δ will always break down (ξ becomes larger than 1) upon lowering T *before* CST sets in. Therefore our results are in fact consistent with previous results.[25,26,29] Furthermore, the functional renormalization group calculation of Ref.[29] reported traces of an "apparent" power law (as opposed to true scaling) that could be linked to the CST mechanism. Finally, Komnik and Gogolin[27] presented an exact solution of a related model at the point $g = 1/2$. In their model, however, there is *no sequential tunneling regime at all*, and therefore we believe that this represents a non generic situation that has nothing to say about the issues at stake here. This point has also been clarified in other recent publications.[28,29] Unfortunately, this also excludes the possibility of an independent analytical check of our results.

To conclude, we hope that these novel features of interacting one-dimensional electrons will stimulate other theoretical work as well as further experimental checks of the CST versus UST picture put forward here.

Acknowledgments

We thank A.O. Gogolin, V. May, Yu. Nazarov, U. Weiss, and especially J. Stockburger for discussions. This work has been supported by the EU network DIENOW, the SFB TR/12, and the Gerhard-Hess program of the DFG.

APPENDIX A: FOURIER EXPANSION SCHEME

To evaluate the rate expressions in Sec. III, we often need the quantities $e^{\pm W_{\rm dot}(t)}$ and $e^{\pm W_\Delta(t)}$. Exploiting the periodicity of these correlation functions with period $\tau_\varepsilon = 2\pi/\varepsilon$, it is convenient to perform a Fourier expansion,

$$\begin{aligned} e^{W_{\rm dot}(t)} &= \sum_{p=-\infty}^{\infty} c_p(\varepsilon) e^{-ip\varepsilon t}, \\ e^{-W_{\rm dot}(t)} &= \sum_{p=-\infty}^{\infty} d_p(\varepsilon) e^{-ip\varepsilon t}, \\ e^{-W_\Delta(t)} &= \sum_{p=-\infty}^{\infty} v_p(\varepsilon) e^{-ip\varepsilon t}, \\ e^{W_\Delta(t)} &= \sum_{p=-\infty}^{\infty} w_p(\varepsilon) e^{-ip\varepsilon t}. \end{aligned}$$

We note that Eqs. (23) and (27) imply that these Fourier coefficients are real. For low temperatures T, but keeping leading corrections in $y = e^{-\varepsilon/T}$, one finds, with the

Heaviside function $\theta(x)$:

$$\begin{aligned}
c_k(\varepsilon,T) &= c_k - \frac{1}{g}y\left(c_{k-1}+c_{k+1}+2c_k\right)+\mathcal{O}(y^2)\,,\\
c_k &= \theta(k)(-1)^k\frac{(1-e^{-\varepsilon/D})^{-1/g}}{k!}\\
&\quad\times\frac{\Gamma(1/g+1)}{\Gamma(1/g-k+1)}e^{-k\varepsilon/D},\\
d_k(\varepsilon,T) &= d_k + \frac{1}{g}y\left(d_{k-1}+d_{k+1}-2d_k\right)+\mathcal{O}(y^2),\\
d_k &= \theta(k)\frac{(1-e^{-\varepsilon/D})^{1/g}}{k!}\frac{\Gamma(1/g+k)}{\Gamma(1/g)}e^{-k\varepsilon/D},\\
v_k(\varepsilon,T) &= (-1)^k\chi c_k(\varepsilon,T),\\
\chi &= \frac{(1+e^{-\varepsilon/D})^{-1/g}}{(1-e^{-\varepsilon/D})^{-1/g}}\,,\\
w_k(\varepsilon,T) &= (-1)^k\chi^{-1}d_k(\varepsilon,T).
\end{aligned}$$

Note that $c_0d_0 = v_0w_0 = 1$. The Fourier coefficients are shown in Figs. 10 and 11 for $g = 0.6$ and $T \ll \varepsilon$. In that case, the $T = 0$ form of the correlation functions (23) and (27) can be taken. Since the number of non zero Fourier coefficients is not exceedingly large, a quick, very accurate, and reliable numerical scheme can be implemented for the evaluation of diagrams of the first class.

Next, as mentioned in Sec. III B, we show in detail how diagrams of the first class ($k = 1, 2, 7, 8$) in Table II have been handled, taking $\Gamma^{f,(2)}_{R,7}(n)$ as concrete example. We consider the expressions on resonance and for low temperature $T \ll \varepsilon$. After inserting the above Fourier expansions, the integration over τ_2 can be performed directly. Since $w_0v_0 = 1$, the '-1' in the square bracket expression in $\Gamma^{f,(2)}_{R,7}$, see Table II, is exactly canceled by the corresponding Fourier term. We find

$$\Gamma^{f,(2)}_{R,7}(n) = -2\frac{\Delta^4}{16}\mathrm{Re}\sum_{k,l=0}^{\infty}{\sum_{m,r,p,q=0}^{\infty}}'\frac{d_kd_lw_mv_rv_pw_q}{\gamma-i\varepsilon_{-mr-pq}}\int_0^\infty d\tau_1 e^{-W^*_{\mathrm{Ohm}}(\tau_1)+i\varepsilon_{-k-mp}\tau_1}\int_0^\infty d\tau_3 e^{-W_{\mathrm{Ohm}}(\tau_3)+i\varepsilon_{-l-pq}\tau_3}\,, \tag{A1}$$

where we have introduced the notation $\varepsilon_{-mr-pq} = (-m+r-p+q)\varepsilon$, and analogously for ε_{-k-mp}. The prime in $\sum'$ indicates that the term with $m = r = p = q = 0$ is excluded from the sum. Next, we define the dimensionless kernels [cf. Eqs. (22) and (25)]

$$\begin{aligned}
K_{\mathrm{R}}(E) &= \varepsilon\int_0^\infty d\tau e^{-S_{\mathrm{Ohm}}(\tau)}\cos\left[E\tau - R_{\mathrm{Ohm}}(\tau)\right]\\
&= \frac{2\varepsilon}{\Delta^2}\Gamma_{\mathrm{Ohm}}(E), \qquad\qquad (A2)\\
K_{\mathrm{I}}(E) &= \varepsilon\int_0^\infty d\tau e^{-S_{\mathrm{Ohm}}(\tau)}\sin\left[E\tau - R_{\mathrm{Ohm}}(\tau)\right],
\end{aligned}$$

such that

$$\begin{aligned}
\Gamma^{f,(2)}_{R,7}(n) = -2\frac{\Delta^4}{16\varepsilon^2}\sum_{k,l=0}^{\infty}{\sum_{m,r,p,q=0}^{\infty}}'\frac{d_kd_lw_mv_rv_pw_q}{\gamma^2+\varepsilon^2_{-mr-pq}}\{&\gamma K_{\mathrm{R}}(-\varepsilon_{kmp})K_{\mathrm{R}}(\varepsilon_{-l-pq}) - \gamma K_{\mathrm{I}}(-\varepsilon_{kmp})K_{\mathrm{I}}(\varepsilon_{-l-pq})\\
&-\varepsilon_{-mr-pq}\left[K_{\mathrm{R}}(-\varepsilon_{kmp})K_{\mathrm{I}}(\varepsilon_{-l-pq}) + K_{\mathrm{I}}(-\varepsilon_{kmp})K_{\mathrm{R}}(\varepsilon_{-l-pq})\right]\}\,.
\end{aligned}$$

Since one needs to self-consistently enforce $\gamma \ll \varepsilon$, we can simplify this expression to the form

$$\Gamma^{f,(2)}_{R,7}(n) = \frac{\Delta^4}{\varepsilon^3}\left(-\frac{\varepsilon}{\gamma}A_{g,7} + \frac{\gamma}{\varepsilon}B_{g,7} + C_{g,7}\right), \tag{A3}$$

with the γ-independent terms

$$
\begin{aligned}
A_{g,7} &= \frac{1}{8}\sum_{k,l=0}^{\infty}{\sum_{r,p,q=0}^{\infty}}' d_k d_l d_{r-p+q} c_r c_p d_q \left\{K_{\rm R}(-\varepsilon_{krq})K_{\rm R}(\varepsilon_{-l-pq}) - K_{\rm I}(-\varepsilon_{krq})K_{\rm I}(\varepsilon_{-l-pq})\right\} \\
B_{g,7} &= -\frac{1}{8}\sum_{k,l=0}^{\infty}{\sum_{m,r,p,q=0}^{\infty}}'' \frac{d_k d_l d_m c_r c_p d_q}{(-m+r-p+q)^2}(-1)^{m+r+p+q}\left\{K_{\rm R}(-\varepsilon_{kmp})K_{\rm R}(\varepsilon_{-l-pq})\right. \\
&\quad \left. -K_{\rm I}(-\varepsilon_{kmp})K_{\rm I}(\varepsilon_{-l-pq})\right\} \\
C_{g,7} &= -\frac{1}{8}\sum_{k,l=0}^{\infty}{\sum_{m,r,p,q=0}^{\infty}}'' \frac{d_k d_l d_m c_r c_p d_q}{-m+r-p+q}(-1)^{m+r+p+q}\left\{-K_{\rm R}(-\varepsilon_{kmp})K_{\rm I}(\varepsilon_{-l-pq})\right. \\
&\quad \left. -K_{\rm I}(-\varepsilon_{kmp})K_{\rm R}(\varepsilon_{-l-pq})\right\} . \qquad \text{(A4)}
\end{aligned}
$$

Here, the second prime in $\sum''$ denotes the sum with the constraint $-m+r-p+q \neq 0$. The remaining Fourier sums are performed numerically.

For completeness, we finally summarize the corresponding results for the remaining diagrams of this type, $k = 1, 2, 8$. The final result for each diagram will be of the form (A3), with $A_{g,1} = A_{g,2} = 0$ and

$$
\begin{aligned}
A_{g,8} &= \frac{1}{8}\sum_{k,l=0}^{\infty}{\sum_{r,p,q=0}^{\infty}}' d_k d_l c_{r-p+q} d_r d_p c_q \left\{K_{\rm R}(-\varepsilon_{krq})K_{\rm R}(\varepsilon_{-lp-q}) + K_{\rm I}(-\varepsilon_{krq})K_{\rm I}(\varepsilon_{-lp-q})\right\} , \\
B_{g,1} &= -\frac{1}{8}\sum_{k,l=0}^{\infty}{\sum_{m,r,p,q=0}^{\infty}}' \frac{d_k d_l d_m c_r c_p d_q}{(m+r+p+q)^2}(-1)^{m+r+p+q}\left\{K_{\rm R}(-\varepsilon_{kmp})K_{\rm R}(\varepsilon_{-lpq})\right. \\
&\quad \left. +K_{\rm I}(-\varepsilon_{kmp})K_{\rm I}(\varepsilon_{-lpq})\right\} , \\
B_{g,2} &= -\frac{1}{8}\sum_{k,l=0}^{\infty}{\sum_{m,r,p,q=0}^{\infty}}' \frac{d_k d_l c_m d_r d_p c_q}{(m+r+p+q)^2}(-1)^{m+r+p+q}\left\{K_{\rm R}(-\varepsilon_{kmp})K_{\rm R}(-\varepsilon_{lpq})\right. \\
&\quad \left. -K_{\rm I}(-\varepsilon_{kmp})K_{\rm I}(-\varepsilon_{lpq})\right\} , \\
B_{g,8} &= -\frac{1}{8}\sum_{k,l=0}^{\infty}{\sum_{m,r,p,q=0}^{\infty}}'' \frac{d_k d_l c_m d_r d_p c_q}{(-m+r-p+q)^2}(-1)^{m+r+p+q}\left\{K_{\rm R}(-\varepsilon_{kmp})K_{\rm R}(\varepsilon_{-lp-q})\right. \\
&\quad \left. +K_{\rm I}(-\varepsilon_{kmp})K_{\rm I}(\varepsilon_{-lp-q})\right\} , \\
C_{g,1} &= -\frac{1}{8}\sum_{k,l=0}^{\infty}{\sum_{m,r,p,q=0}^{\infty}}' \frac{d_k d_l d_m c_r c_p d_q}{m+r+p+q}(-1)^{m+r+p+q}\left\{-K_{\rm R}(-\varepsilon_{kmp})K_{\rm I}(\varepsilon_{-lpq})\right. \\
&\quad \left. -K_{\rm I}(-\varepsilon_{kmp})K_{\rm R}(\varepsilon_{-lpq})\right\} , \\
C_{g,2} &= -\frac{1}{8}\sum_{k,l=0}^{\infty}{\sum_{m,r,p,q=0}^{\infty}}' \frac{d_k d_l c_m d_r d_p c_q}{m+r+p+q}(-1)^{m+r+p+q}\left\{K_{\rm R}(-\varepsilon_{kmp})K_{\rm I}(-\varepsilon_{lpq})\right. \\
&\quad \left. +K_{\rm I}(-\varepsilon_{kmp})K_{\rm R}(-\varepsilon_{lpq})\right\} , \\
C_{g,8} &= -\frac{1}{8}\sum_{k,l=0}^{\infty}{\sum_{m,r,p,q=0}^{\infty}}'' \frac{d_k d_l c_m d_r d_p c_q}{-m+r-p+q}(-1)^{m+r+p+q}\left\{K_{\rm R}(-\varepsilon_{kmp})K_{\rm I}(\varepsilon_{-lp-q})\right. \\
&\quad \left. -K_{\rm I}(-\varepsilon_{kmp})K_{\rm R}(\varepsilon_{-lp-q})\right\} . \qquad \text{(A5)}
\end{aligned}
$$

Finally, we explain why we expect $C_g(T)$ to be T independent, focusing on diagrams of the first class ($k = 1, 2, 7, 8$). Using Eqs. (A4) and (A5), the only T-dependent terms are the $K_{\rm R/I}(E)$ defined above. Al-

though $K_R(E=0)$ has a power-law T dependence with $K_R(E=0) \propto T^{1/g-1}$, for finite energies $E \gg T$, and hence for $T \ll \varepsilon$, the T dependence is exponentially suppressed since the finite level spacing acts as an effective energy bias, see Eqs. (A3) and (25). Similar arguments apply to $K_I(E)$, which can be evaluated numerically in a straightforward manner. Although no closed analytical expression can be given, the overall T dependence follows directly from these considerations.

[1] S. Tomonaga, Prog. Theor. Phys. **5**, 544 (1950).
[2] J.M. Luttinger, J. Math. Phys. **4**, 1154 (1963).
[3] K. Schönhammer, J. Phys.: Condens. Matter **14**, 12783 (2002).
[4] T. Giamarchi, *Quantum Physics in One Dimension* (Clarendon, Oxford 2004).
[5] O.M. Auslaender, A. Yacoby, R. de Picciotto, K. W. Baldwin, L. N. Pfeiffer, and K. W. West, Phys. Rev. Lett. **84**, 1764 (2000).
[6] A.M. Chang, Rev. Mod. Phys. **75**, 1449 (2003).
[7] C. Dekker, Phys. Today **52** (5), 22 (1999).
[8] R. Egger and A.O. Gogolin, Phys. Rev. Lett. **79**, 5082 (1997); Eur. Phys. J. B **3**, 281 (1998).
[9] C. Kane, L. Balents, and M.P.A. Fisher, Phys. Rev. Lett. **79**, 5086 (1997).
[10] M. Bockrath, D.H. Cobden, J. Lu, A. G. Rinzler, R. E. Smalley, L. Balents, and P. McEuen, Nature (London) **397**, 598 (1999).
[11] Z. Yao, H.W.Ch. Postma, L. Balents, and C. Dekker, Nature (London) **402**, 273 (1999).
[12] J. Nygård, D.H. Cobden, M. Bockrath, P.L. McEuen, and P.E. Lindelof, Appl. Phys. A **69**, 297 (1999).
[13] H.W.Ch. Postma, M. de Jonge, Z. Yao, and C. Dekker, Phys. Rev. B **62**, R10653 (2000).
[14] C.L. Kane and M.P.A. Fisher, Phys. Rev. B **46**, 15233 (1992).
[15] H.W.Ch. Postma, T. Teepen, Z. Yao, M. Grifoni, and C. Dekker, Science **293**, 76 (2001).
[16] D. Bozovic, M. Bockrath, J.H. Hafner, C. M. Lieber, H. Park, and M. Tinkham, Appl. Phys. Lett. **78**, 3693 (2001).
[17] I.O. Kulik and R.I. Shekhter, Sov. Phys. JETP **4**, 308 (1975).
[18] C.W.J. Beenakker, Phys. Rev. B **44**, 1646 (1991).
[19] G.L. Ingold and Yu.V. Nazarov, in *Single Charge Tunneling*, NATO ASI Ser. B **294**, ed. by H. Grabert and M.H. Devoret (Plenum, New York 1992).
[20] A. Furusaki and N. Nagaosa, Phys. Rev. B **47**, 3827 (1993).
[21] M. Sassetti, F. Napoli, and U. Weiss, Phys. Rev. B **52**, 11213 (1995).
[22] A. Furusaki, Phys. Rev. B **57**, 7141 (1998).
[23] A. Braggio, M. Grifoni, M. Sassetti, and F. Napoli, Europhys. Lett. **50**, 236 (2000).
[24] M. Thorwart, M. Grifoni, G. Cuniberti, H.W.Ch. Postma, and C. Dekker, Phys. Rev. Lett. **89**, 196402 (2002).
[25] Yu.V. Nazarov and L.I. Glazman, Phys. Rev. Lett. **91**, 126804 (2003).
[26] D.G. Polyakov and I.V. Gornyi, Phys. Rev. B **68**, 035421 (2003).
[27] A. Komnik and A.O. Gogolin, Phys. Rev. Lett. **90**, 246403 (2003).
[28] S. Hügle and R. Egger, Europhys. Lett. **66**, 565 (2004).
[29] V. Meden, T. Enss, S. Andergassen, W. Metzner, and K. Schönhammer, Phys. Rev. B **71**, 041302 (R) (2005).
[30] U. Weiss, *Quantum Dissipative Systems*, 2nd edition (World Scientific, Singapore, 1999).
[31] Y. Hu and S. Mukamel, J. Chem. Phys. **91**, 6973 (1989).
[32] R. Kubo, M. Toda, and N. Hashitsume, *Statistical Physics II*, Springer Series in Solid State Physics, Vol. 31 (Springer, Berlin, 1985).
[33] V. Weisskopf and E. Wigner, Z. Phys. **63**, 54 (1930).
[34] R. Zwanzig, Physica (Amsterdam) **30**, 1109 (1964).
[35] W.H. Press *et al.*, *Numerical Recipes in FORTRAN* (Cambridge University Press, Cambridge, England 1992).
[36] H. Baur, A. Fubini, and U. Weiss, Phys. Rev. B **70**, 024302 (2004).
[37] There is no need to neglect the dipole-dipole correlations Λ_{ij}^{Σ} in Ref. 24, when the higher-order contributions are summed up.

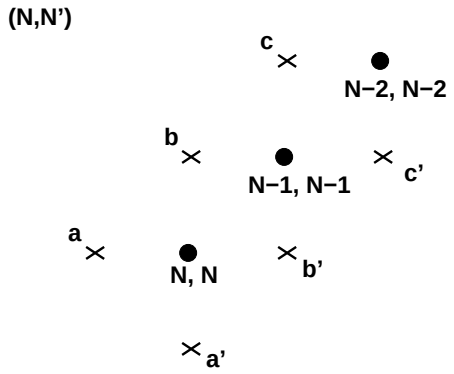

FIG. 1: Relevant part of the (N, N')-plane of the RDM (schematic). Diagonal states are indicated by filled circles, off-diagonal states are marked by crosses. We use the shorthand notation $a = (N, N+1), b = (N-1, N)$, and $c = (N-2, N-1)$, and complex conjugate states are indicated by the prime. For the irreducible Γ_0^2 contribution to the $N \to N-1$ rate, we have four jumps. One starts from (N, N) and ends in $(N-1, N-1)$, visiting an intermediate diagonal state after every second jump.

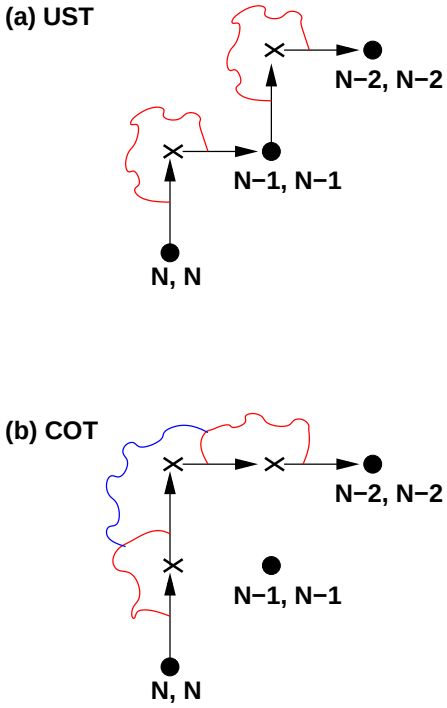

FIG. 2: (Color online) Paths in the RDM for (a) uncorrelated sequential tunneling (UST), and (b) cotunneling (COT). Wiggled lines schematically indicate "bath-induced" correlations for first (red)- and second (blue)-order transitions in Γ_0. Diagram (a) involves two irreducible golden rule transition rates, i.e., there are no correlations across the intermediate diagonal state. Diagram (b) is not considered in what follows since we study a conductance peak.

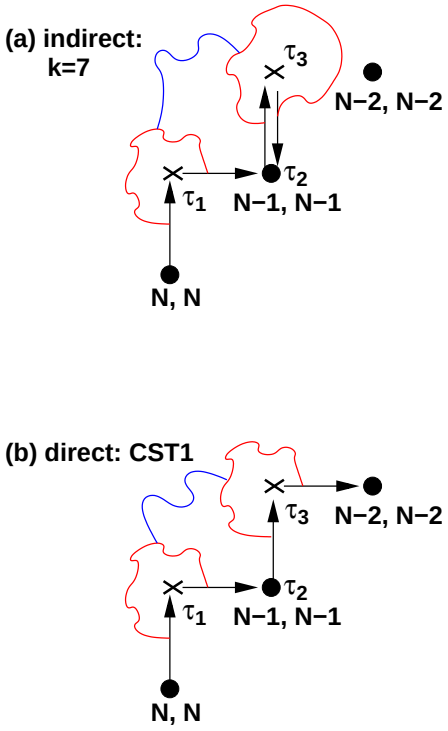

FIG. 3: (Color online) Examples for CST diagrams of order $\Gamma_0^2 \propto \Delta^4$: (a) the "indirect" diagram $k = 7$ in Tables I and II and (b) the "direct" diagram CST1.

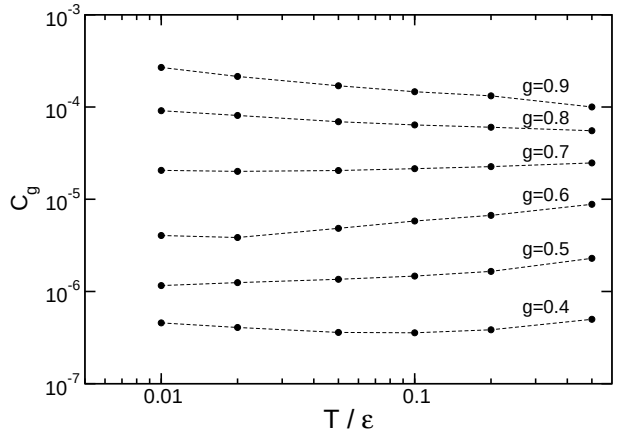

FIG. 4: Temperature dependence of the dimensionless parameter C_g in Eq. (29) for various g and $D = 10\varepsilon$. Dashed lines are guides to the eye only. Notice the double-logarithmic scales.

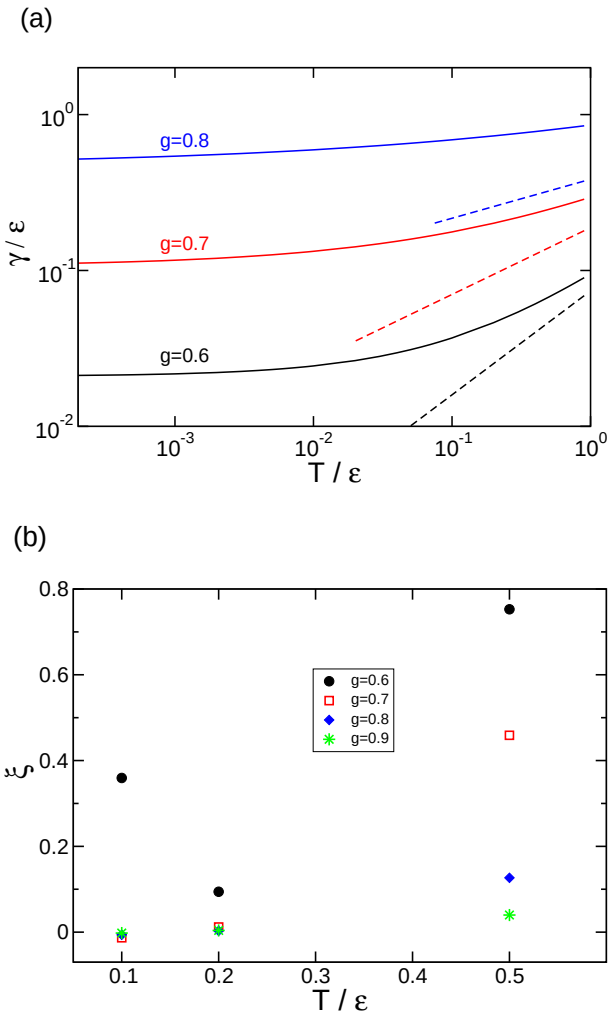

FIG. 5: (Color online) (a) Linewidth γ and (b) the parameter ξ in Eq. (33) as a function of T for different g at $\Delta = 6\varepsilon$, $D = 10\varepsilon$. Dashed lines in (a) represent $4\Gamma^{(1)} \propto T^{-1+1/g}$. Notice the double-logarithmic scales. (Using these parameters, the master equation approach breaks down for $g = 0.9$.)

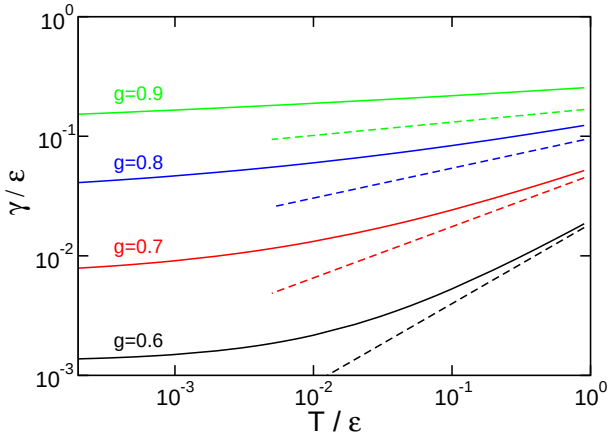

FIG. 6: (Color online) Same as Fig. 5(a), but for $\Delta = 3\varepsilon$.

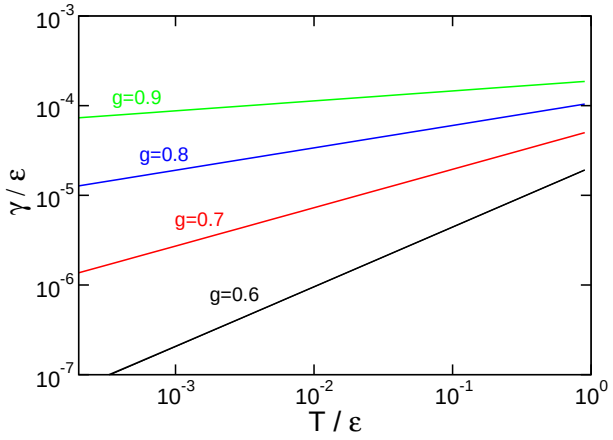

FIG. 7: (Color online) Same as Fig. 6, but for $\Delta = 0.1\varepsilon$. Dashed lines describing $4\Gamma^{(1)}$ coincide with the full result for γ.

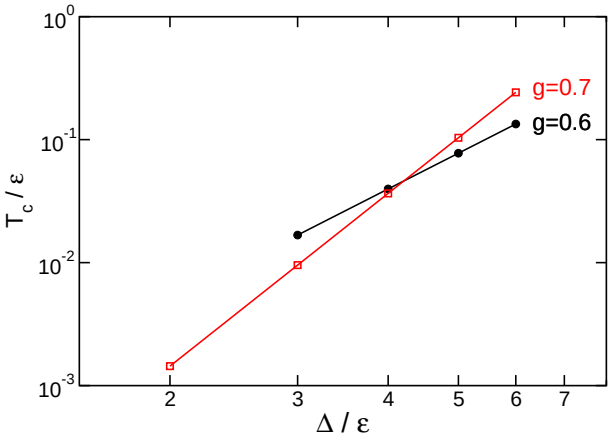

FIG. 9: Crossover temperature T_c separating the UST ($T > T_c$) and CST ($T < T_c$) regimes ($D = 10\varepsilon$) for different Δ and $g = 0.6, 0.7$.

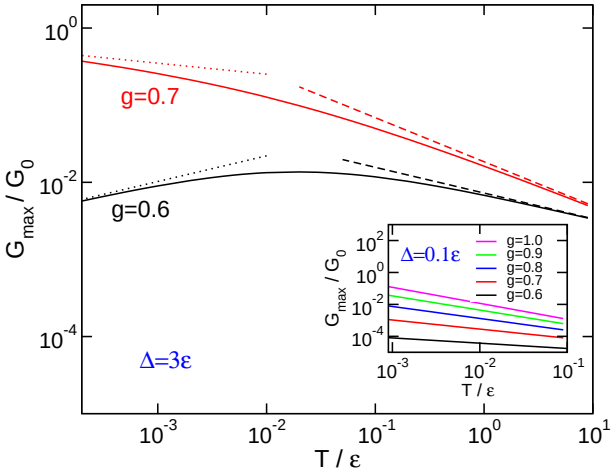

FIG. 8: (Color online) Temperature dependence of the conductance maximum $G_{\max}$ (solid lines) for $\Delta = 3\varepsilon$ and TLL parameters $g = 0.6$ and $g = 0.7$. Note the double-logarithmic scales. Dotted (dashed) lines represent the CST (UST) power law $G_{\max} \propto T^{\alpha_{\rm CST}}$ ($G_{\max} \propto T^{\alpha_{\rm UST}}$). Inset: $G_{\max}$ for $\Delta = 0.1\varepsilon$ and g between $g = 0.6$ (bottom) and $g = 1.0$ (top). The slopes coincide with $\alpha_{\rm UST} = -2 + 1/g$.

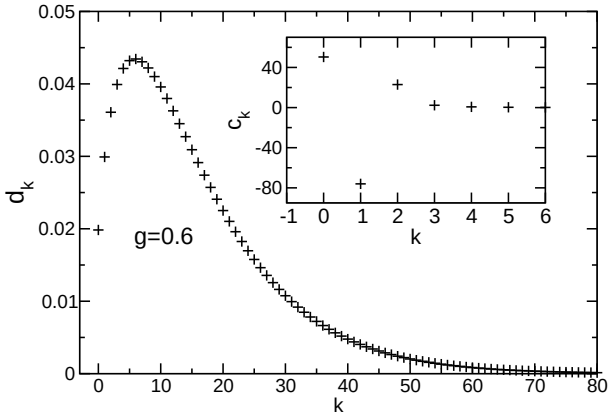

FIG. 10: Fourier components d_k and c_k (inset) for $g = 0.6$ and $T \ll \varepsilon$.

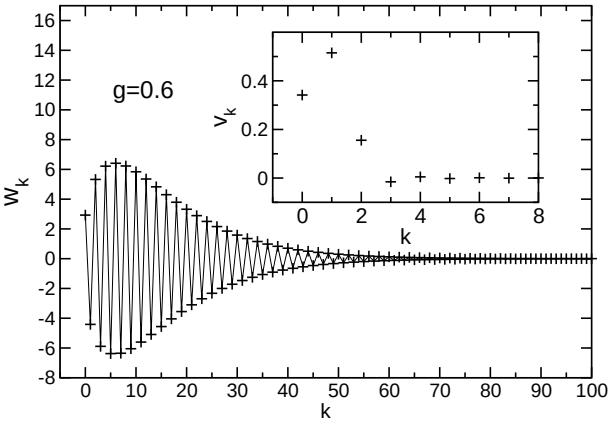

FIG. 11: Same as Fig. 10 but for the Fourier components w_k and v_k (inset).